Energy & Environmental Science

Organic Emitters with Near-Unity Photoluminescence to Reinforce Buried Interface of Perovskite Solar Cells and Modules

Journal:	*Energy & Environmental Science*
Manuscript ID	EE-REV-04-2024-001552.R1
Article Type:	Paper
Date Submitted by the Author:	24-May-2024

Complete List of Authors:	Suo, Zhen-Yang ; Lanzhou University Xiao, Guobin ; Lanzhou University Su, Zhenhuang; c. Shanghai Synchrotron Radiation Facility (SSRF), Shanghai Advanced Research Institute, Chinese Academy of Sciences Dong, Runmin ; Lanzhou University Mu, Xijiao ; Lanzhou University Gao, Xingyu; c. Shanghai Synchrotron Radiation Facility (SSRF), Shanghai Advanced Research Institute, Chinese Academy of Sciences Wu, Yiying; The Ohio State University Cao, Jing; Lanzhou University, College of Chemistry and Chemical Engineering

SCHOLARONE™
Manuscripts

Precise manipulation of the interfacial contacts and defects at buried perovskite-substrate interface remains a persistent challenge in the pursuit of highly efficient and stable solar cells and solar modules. In this study, we develop a buried interface reinforcement strategy employing cyano-based organic emitters with near-unity photoluminescence efficiency. Owing to the dipole homogenization effect, the electron distribution around the cyano group in triphenylamine-based emitters becomes more dispersed, rendering it highly effective in compensating iodide vacancies and reinforcing the PbI_6 octahedral configuration at the buried interface. This emitter with near-unity photoluminescence further mitigates photochemical degradation during prolonged illumination, thus enhancing device performance and stability. Devices with an active area of 0.10 cm^2 achieved a champion efficiency of up to 25.67% (certified 25.09%), while solar modules reached record efficiencies of 23.41% (certified 22.83%) and 21.91% for aperture areas of 11.44 cm^2 and 72.00 cm^2, respectively. An unencapsulated device maintained 90% of its initial performance after 1000 hours of continuous 1-sun illumination at maximum power point operating conditions. This work offers a promising strategy for enhancing the performance and stability of perovskite solar cells and modules by buried interface manipulation.

ARTICLE

Organic Emitters with Near-Unity Photoluminescence to Reinforce Buried Interface of Perovskite Solar Cells and Modules

Received 00th January 20xx,
Accepted 00th January 20xx

DOI: 10.1039/x0xx00000x

Zhen-Yang Suo[a,†], Guo-Bin Xiao[a,†], Zhenhuang Su[b,†], Runmin Dong[a], Xijiao Mu[a], Xingyu Gao[b], Yiying Wu[c], Jing Cao[a,*]

Stabilizing the imbedded perovskite-substrate interface without UV-vis damage is still a long-enduring challenge in perovskite solar cells and modules, since it brings energy loss and phase instability under UV-vis illumination. In this work, we develop a buried interface reinforcement strategy by cyano-based organic emitters with near-unity photoluminescence. Due to the dipole homogenization effect, the electron distribution around cyano group in triphenylamine-based emitter is more dispersed, making it better suited to compensate the iodide vacancies and reinforce PbI_6 octahedral configuration at the buried interface. This emitter with near-unity photoluminescence further suppresses the photochemical degradation during long-term illumination, contributing to better cell performance and stability. Devices with the active area of 0.10 cm^2 obtain a champion efficient up to 25.67% (certified 25.09%), while the record efficiency of solar modules reaches 23.41% (certified 22.83%) and 21.91% for the aperture area of 11.44 cm^2 and 72.00 cm^2. An unencapsulated device retains 90% of its original performance after 1000 hours under continuous 1-sun illumination at maximum power point operating condition.

Introduction

Solution-processed lead halide polycrystalline perovskite solar cells (PSCs) have reached over 26% power conversion efficiencies (PCEs)[1-7], approaching the best performance of state-of-the-art crystalline-silicon solar cells[8]. In the configuration of PSCs, the perovskite layer is sandwiched between the hole/electron transport layers[9], which play the crucial role for the perovskite nucleation and heterojunction generation[10, 11]. Heterojunction contacts between perovskite and carrier transport layers inevitably influence the cell performance and stability[12], rather than perovskite active or charge transport materials. Additionally, the crystalline property of solution prepared perovskite film causes an even higher defect concentration, particularly deep charge traps at the buried perovskite-substrate interface[13-19]. These defects usually cause the interfacial recombination, and initialize degradation under moisture, oxygen, high temperature, particularly ultraviolet (UV) light since it can be easily induced to yield the irreversible chemical reaction[20-29]. Therefore, it is necessary to manipulate the interfacial contact and defects at the buried interface for the fabrication of highly efficient and stable PSCs, particularly for solar modules[30-34].

There is a diversity of findings in reports on the manipulation of imbedded perovskite-bottom interface[35-39]. The preparation of new electron transport materials, such as lattice-matched oxide perovskite ($SrSnO_3$), enables the more ordered growth of perovskite film. It avoids the generation of a deteriorated buried interface to suppress interfacial defects formation[40]. Introducing the additives into perovskite precursor solution[41-44] or electron transport material[45] have attributed to modulate interfacial heterojunction contact, to minimize interfacial defects, realize superior interface contacts and matched energy levels between perovskite and electron transport layer. Buried interfacial passivation by using a thin layer of two- and three-dimensional (2D/3D) hybrid structures is also beneficial to cell stability[46, 47], contributable to the increased resistance of perovskite degradation by 2D overlayer. Modification of UV-sunscreen passivators at the interface of perovskite and electron transport material also reduce the poor interfacial contact and reduce the corrosion effect of UV on PSCs[26]. However, the reinforcement of buried interfacial PbI_6 octahedral configuration without UV further damage is highly demanded while yet realized for preparing efficient solar cells and modules.

Studies revealed that the donor-π-acceptor molecules with carbazole- or triphenylamine-based donor units and cyano-decorated tetraphenylbenzene core as acceptors have high UV molar absorption coefficient and photoluminescence quantum yields[48, 49]. Moreover, cyano group could connect with Pb in perovskite to compensate iodide vacancies[50-52]. In this work, two cyano-based organic emitters with fluorescence quantum yield over 98% are used to modify at the interface of SnO_2 and perovskite layers (Fig. 1a). The emitters are efficiently bound at the buried interface by the connection of

[a] State Key Laboratory of Applied Organic Chemistry, Key Laboratory of Nonferrous Metal Chemistry and Resources Utilization of Gansu Province, College of Chemistry and Chemical Engineering, Lanzhou University, Lanzhou 730000, P.R. China E-mail: caoj@lzu.edu.cn
[b] Shanghai Synchrotron Radiation Facility (SSRF), Shanghai Advanced Research Institute, Chinese Academy of Sciences, 239 Zhangheng Road, Shanghai 201204, China
[c] Department of Chemistry and Biochemistry, The Ohio State University, 100 West 18th Avenue, Columbus, Ohio 43210, United States
Electronic Supplementary Information (ESI) available: [details of any supplementary information available should be included here]. See DOI: 10.1039/x0xx00000x

cyano groups from emitter and lead in perovskite. By altering the donor units, results reveal that the electron distribution around cyano group in triphenylamine-based emitter are more dispersed, making it better suited to compensate the iodide vacancies and reinforce PbI_6 octahedral configuration. A champion efficient of devices is up to 25.67% with the active area of 0.10 cm^2. The record efficiency of solar modules reaches up to 23.41% (certified at 22.83%) and 21.91% for the aperture area of 11.44 cm^2 and 72.00 cm^2[53]. The emitters with over 98% fluorescence quantum yield effectively convert harmful UV light into infrared light without damage to PSCs, the devices reveal remarkably enhanced stability, especially for UV stability.

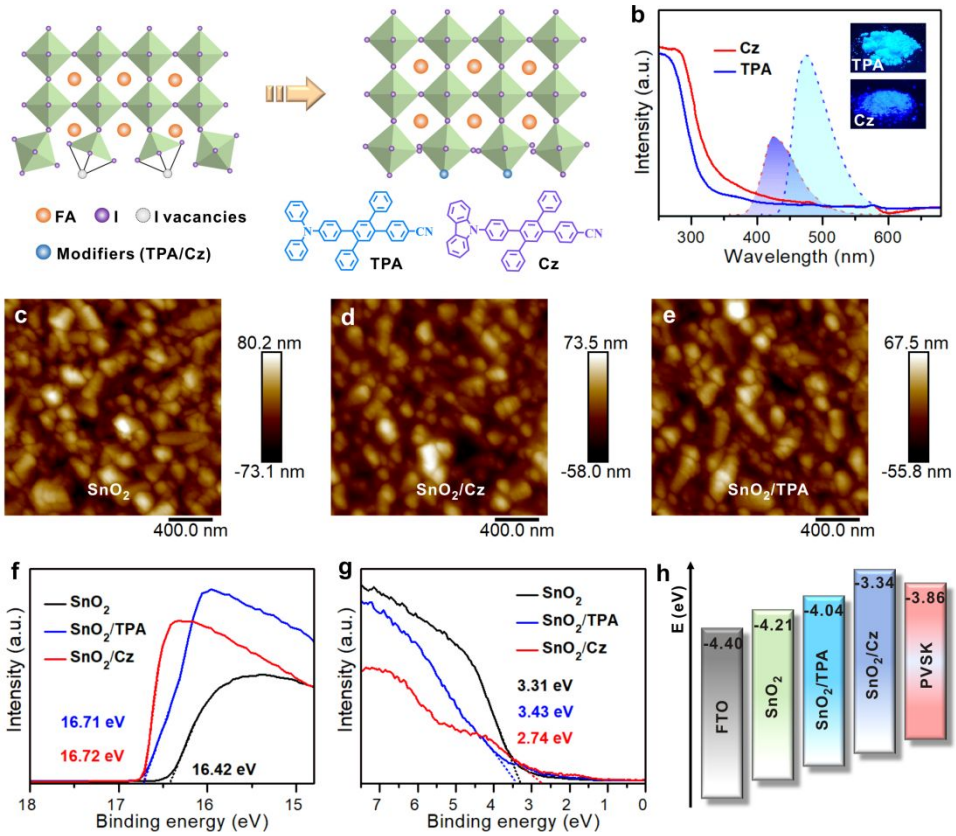

Fig. 1 (a) Schematic diagram of buried surface modified by emitters. (b) UV-Vis absorption, photoluminescence spectra and photoluminescence picture of emitters. AFM images of SnO_2 films without (c), with Cz (d) and TPA (e) treatment. UPS spectra of secondary electron cut-off region (f) and valence band region (g) for SnO_2 films without and with emitters. (h) Energy level scheme of device.

Results and discussion

Substrate modification and its property

Two cyanogen-based emitters bearing carbazole- (Cz) and triphenylamine- (TPA) groups selected as functional skeleton were prepared by the reported methods. Ultraviolet-visible (UV-Vis) absorption spectra at solid state were tested and shown in Fig. 1b. The maximum absorption peaks are located at 274 nm for Cz and 258 nm for TPA, while the emission peaks are 424 nm for Cz and 473 nm for TPA. Notably, the photoluminescence (PL) quantum yields of Cz and TPA at solid state are evaluated being 99.8% for Cz and 98.6% for TPA, revealing the near-unity UV photoluminescence[48, 49]. These results suggest the prepared emitters would realize the efficient UV absorption and highly efficient visible light conversion, to decrease the device destruction by UV radiation. The obtained emitters were then deposited on the SnO_2-coated Fluorine-doped Tin Oxide (FTO) substrate. Scanning electron microscope (SEM) and atomic force microscopy (AFM) tests were conducted to evaluate the effect of emitters on substrate film morphology. As shown in Fig. 1c-e, Fig. S1 and S2 (ESI†), the coating of emitters significantly makes the substrate surface more uniform, reflecting by the root mean square (RMS) of 21.8 nm, 18.0 nm and 17.9 nm for substrates without and with Cz and TPA, respectively. Ultraviolet photoelectron spectroscopy (UPS) measurements were further performed to assess the energy band structure and work function (WF) of substrates. The WF of substrates without and with Cz and TPA were calculated as -4.80 eV, -4.50 eV and -4.51 eV, respectively, while their conduction band minimum (E_{CBM}) values were -4.21 eV, -3.34 eV and -4.04 eV, for substrates without and with Cz and TPA, respectively (Fig. 1f, g). Therefore, the TPA-manipulated substrate has higher conduction band energy level than pure SnO_2 samples, approaching the value of perovskite to facilitate the interfacial charge extraction and transport (Fig. 1h). Similar transmittance values of SnO_2 films without and with emitters indicate that the introduced emitters do not influence the films transmittance (Fig. S3, ESI†).

Characterization analyses of perovskite films

This journal is © The Royal Society of Chemistry 20xx

Please do not adjust margins

The perovskite films were then deposited on as-prepared substrates. The contact angle of perovskite precursor solution on the modified substrate does not change obviously, which indicates that perovskite solution has good infiltration on the modified substrates (Fig. S4, ESI†). There has no UV-vis peaks of emitters in the N,N-Dimethylformamide (DMF) solution containing emitters (Fig. S5, ESI†), suggesting the coated emitters on the SnO_2/FTO substrates are not removed during the prepared process of perovskite layer by solution-process. Although the perovskite crystallites are similar (Fig. S6, ESI†), the perovskite films with emitters have more uniform surface morphology, reflecting by the reduced RMS values (29.2 nm, 27.4 nm and 28.4 nm for samples without, with Cz and TPA, respectively, Fig. 2a-c and Fig. S7, ESI†). The films modified by emitters reveal the relatively enhanced X-ray diffraction (XRD) peaks of perovskite than the pristine sample (Fig. S8, ESI†), which is further demonstrated by Grazing incidence wide-angle X-ray scattering (GIWAXS) patterns. As shown in Fig. 2d-f, a predominant (100) plane of perovskite is at q ≈ 10 nm^{-1} along with q ≈ 9.1 nm^{-1} for a (001) plane of PbI_2. The perovskite films based on emitters show the relatively weakened intensity of PbI_2, while the intensities of perovskites are enhanced. These results indicate that the introduction of emitters contributes to the preparation of high-quality perovskite films.

Crystallization kinetics of perovskite films were then investigated by *in situ* synchrotron radiation GIWAXS measurements. The kinetic processes of perovskite films were mainly defined as two periods illustrated in Fig. 2g-i. During the initial stage, the scattering signal in the q around 8.5 nm^{-1} can be assigned to the yellow intermediate phase of perovskite. During the second stage, the diffraction signal of intermediate phase disappeared, while the α-phase of CsFA-perovskite signal in the q around 10.0 nm^{-1} quickly emerged with the shortened intermediate phase of perovskite. After a certain period, the α-phase perovskite film became purer with minimal occurrence of other unstable phases. Results revealed that the intermediate phase of control perovskite was lasted for approximately 16 seconds after the addition of antisolvent. Whereas the samples based on Cz and TPA exhibited a solvated phase duration of less than 10 seconds (Fig. S9 and 10, ESI†) and the shortened intermediate phase time (Fig. 2g-i). This indicates that the incorporation of emitters facilitates the formation of intermediate phases more effectively and accelerates the generation of light-absorbing α-phase perovskite film[54, 55]. Additionally, compared to the control film, the target films exhibited the smaller peak width after crystal growth cessation (Fig. 2g-i), indicating that the modified perovskite films are more ordered. We can thus conclude that the introduction of emitters accelerate both the crystallization and phase transition to obtain the high-quality perovskite films.

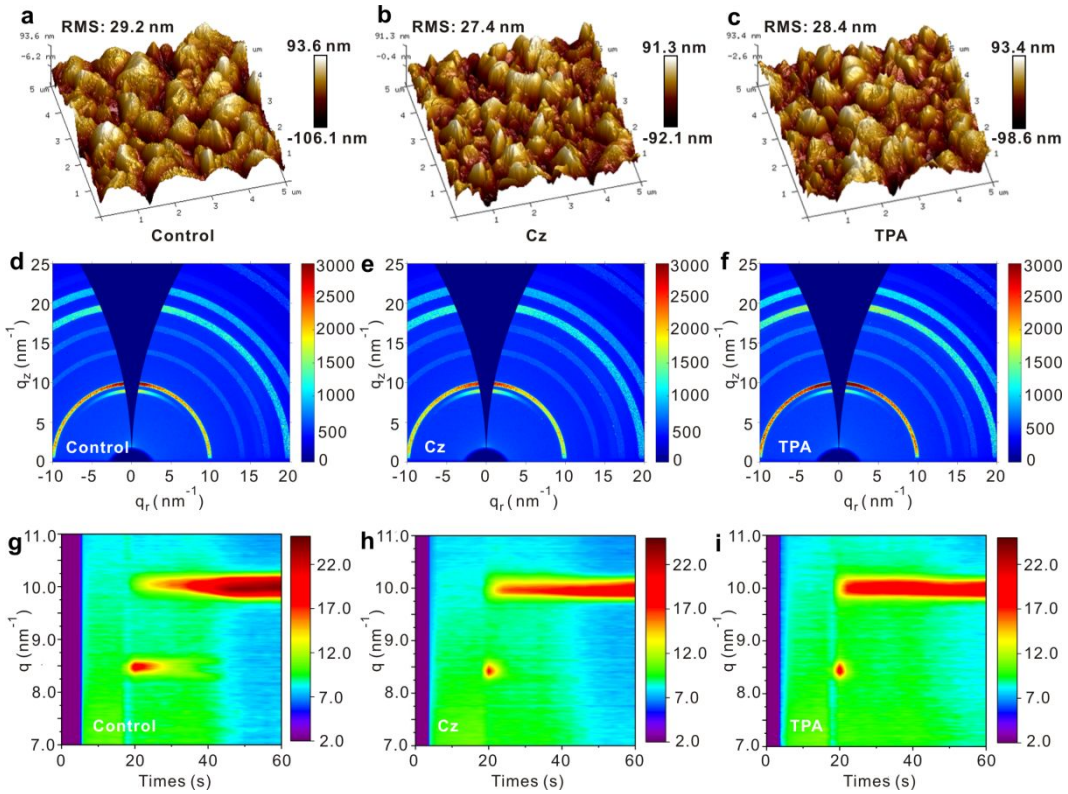

Fig. 2 AFM images of perovskite films without (a), with Cz (b) and TPA (c). 2D GIWAXS images with the x-ray incidence angle at 0.5° of perovskite films for control (d), with Cz (e) and TPA (f). In situ GIWAXS measurements of perovskite films forming process for the control (g), with Cz (h) and TPA (i).

Interfacial interaction analyses

To assess the interaction between cyano unit in emitters and perovskite, X-ray photoelectron spectroscopy (XPS) of perovskite samples with and without emitters were tested. As illustrated in Fig. 3a, b, compared to the perovskite sample, the shift of I and Pb peaks for the emitter-modified perovskite sample was observed. Moreover, the N peaks of emitters were

also shifted than the pristine emitters (Fig. 3c). These shifts indicate the emitters are efficiently bound at the perovskite-bottom surface by the connection of cyano unit and Pb from perovskite. FT-IR spectra revealed the shift of -CN peaks for the modified perovskite sample indicates the presence of interact between the cyano unit and Pb from perovskite (Fig. S11, ESI†). To clearly understand the effect of emitters on the buried interface, the perovskite layers were successfully peeled off from the SnO_2-based substrate, to fully expose the buried interface of perovskite film (Fig. 3d, detailed methods shown in Supplementary section). SEM images revealed that the obvious voids were yielded at the buried interface of control sample (Fig. 3e). By contrast, the voids were substantially decreased in the target buried interface, particularly at the bottom surface of TPA-based sample (Fig. 3f, g). This indicates that the voids at the buried interface probably result from the initial disorder in perovskite lattice, and they can be mitigated by interfacial manipulation to generate a more orderly initiation of perovskite film crystallization. Similar trends were observed under laser confocal laser scanning fluorescence microscopy (CLSFM). The non-uniformity fluorescence distribution with many dark areas was observed for the control sample (Fig. 3h). In comparison, the target samples (especially for TPA-based sample) exhibited the more uniform and brighter fluorescence (Fig. 3i, j), verifying the presence of better film crystallization at their imbedded bottom interfaces. The largest fluorescence intensity of TPA-based film excited from substrate bottom than the control and Cz-based sample further demonstrates above results (Fig. S12, ESI†). Thus, the emitters could stabilize the buried interface by modulating the interfacial perovskite film crystallization to yield the high-quality perovskite films.

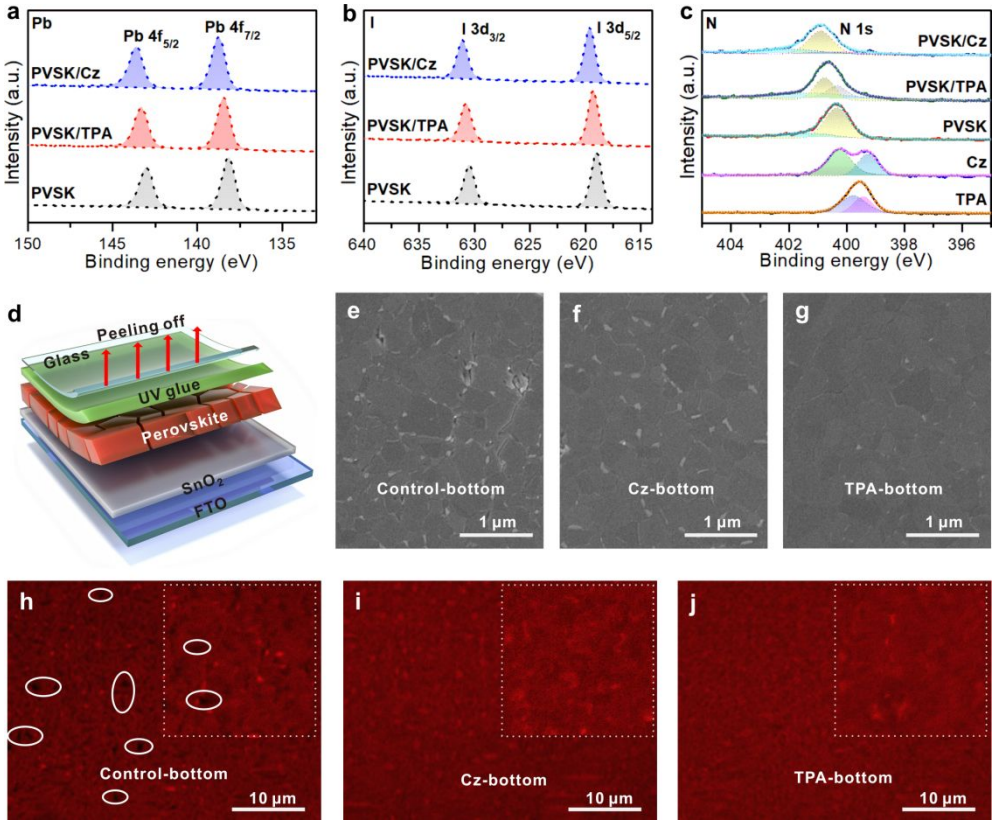

Fig. 3 XPS spectra of Pb 4f (a), I 3d (b), N 1s (c) for perovskite samples without, with Cz and TPA. (d) Schematic diagram of peeling off the buried interface from device (e-g). SEM images of perovskite films without (e) and with Cz (f) and TPA (g) from bottom side. CLSFM images of perovskite films without (h) and with Cz (i) and TPA (j) from bottom side.

A series of experimental analyses were then prepared to evaluate the positive function on interfacial defects and charge transport property. There are not changed UV-vis spectra of perovskite films with and without emitters (Fig. S13, ESI†), suggesting that the introduction of emitters do not change the optical property of perovskite films. Compared to the control sample, the emitters-modified perovskite films have enhanced fluorescence intensities, especially for TPA-coated sample (Fig. S12a, ESI†). This suggests the TPA-modified film facilitate the preparation of high-quality perovskite film. Defect state density of emitters-based devices was tested by space-charge-limited current (SCLC) method and shown in Fig. S14a (ESI†). The TPA- and Cz-based samples have similar values being 7.26 × 10^{14} cm^{-3} and 1.45 × 10^{15} cm^{-3}, respectively, much lower than that of control sample with 6.05 × 10^{15} cm^{-3}. Urbach energy values of the modified perovskite films are smaller than that of control sample (Fig. S15, ESI†) exhibits the modification of emitters improves the quality of perovskite films with fewer defects[56]. Mott-Schottky tests were conducted to evaluate the interfacial charge transport property[57]. As displayed in Fig. S14b (ESI†), the TPA-treated sample exhibits the largest slope than those of the Cz-based device and control sample, indicating the existence of lower interface charge density in TPA-treated sample. Additionally, compared to the Cz-

This journal is © The Royal Society of Chemistry 20xx

Please do not adjust margins

modified device and control sample, the largest recombination resistance for the TPA-treated sample indicates the presence of reduced interfacial charge recombination for the TPA-treated sample (Fig. S14c, ESI†). Thus, the TPA treatment can reduce defects and boost interfacial charge transport.

Theoretical analysis.

Structural and electronic transport behavior of emitters at the buried interface was performed using Density Functional Theory (DFT). Electrostatic potential surfaces of emitters reveal the lower potential at cyano group end and the positive potential at the opposite end, exhibiting the significant dipole moment (Fig. 4a, b). In Cz molecule, the in-plane dipole contribution is counteractive to the overall molecular dipole. Whereas non-planar phenyl groups' torsion aligns the dipole components outward in TPA, to enhance the molecule's total dipole moment. Consequently, TPA molecule's total dipole moment (6.13 Debye) is larger than that of Cz (3.73 Debye), as shown in Fig. 4c, d and Fig. S16 and Table 1 (ESI†). The stronger dipole results in larger atomic basin of cyano unit in TPA (32.46 Å^3) than that of Cz (25.41 Å^3) (Fig. 4e, f). This situation makes TPA molecule more favorable for filling the I vacancies to well reinforce PbI_6 octahedral configuration at buried surface. Restrained electrostatic potential (RESP) charge (Table S2) calculations point out that the lesser electron transfer from cyano group in TPA to Pb in PbI_6 octahedron than in Cz system, resulting in a larger Pb-N distance and a more intrinsic-like Pb-I octahedron structure (Fig. 4h, i). This defect-filling way encourages the reconstruction of a cubic phase at perovskite surface (Table S3).

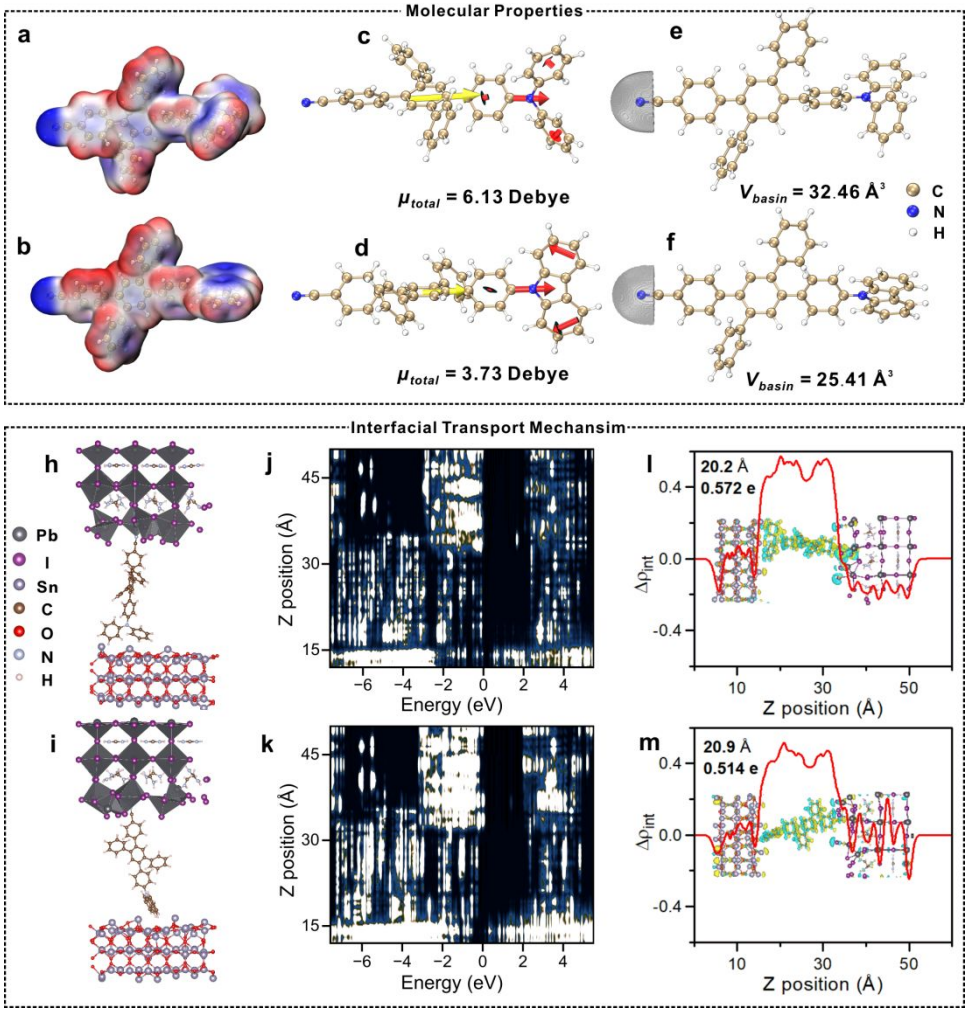

Fig. 4 (a) Molecular surface electrostatic potential (a, b), fragment dipole moment (c, d) and cyano atomic basin analysis (e, f) for TPA and Cz. Optimized geometry structures (h, i), PLDOS (j, k) and electron transfer curve and isosurface (l, m) at the interface of perovskite and emitters (TPA and Cz).

Additionally, the TPA-modified perovskite surface displays superior electronic transport states (Energy = 0), thus augmenting the electronic transport efficiency of the resultant interface system. Specifically, in the presence of Energy = 0, the TPA system harbors electronic states facilitating charge transport. In contrast, the absence of such electronic states in the Cz system attenuates the related transmission. (Fig. 4j, k). Electron transfer analysis demonstrates that the TPA-based interface facilitates greater electron transfer (0.572 e) compared to the Cz system (0.514 e). The increased electron transfer values stem from the integration of curves in Fig. 4l, m, indicating a higher efficiency of charge transfer performance. In conclusion, the torsion of the phenyl groups in TPA counteracts the reduction in the total molecular dipole,

resulting in a stronger molecular dipole and an enlarged atomic basin. Modification at the perovskite and SnO_2 interfaces with TPA stabilizes perovskite lattice and enhances electronic transport properties.

Photovoltaic performance and stability analyses of devices

We utilized the emitters-modified SnO_2 substrates to fabricate n-i-p-structured PSCs with FTO/SnO_2/Cz or TPA/perovskite/Spiro-OMeTAD/Au configuration in ambient air (Fig. S17, ESI†). Performance tests of minimal small cells with the active area being 0.1 cm^2 revealed that the optimal coating concentration of emitters in dichloromethane solution is 0.3 mg/ml (Fig. 5a and Fig. S18, ESI†). As expected, the champion TPA-based PSCs with negligible hysteresis obtained a notable performance up to 25.67%/25.12% (reverse/forward scan direction), whereas the best efficiency of Cz-based and control devices were 24.65%/24.26% and 23.58%/23.15% (Fig. 5b and Table S4, ESI†). A PCE of 25.09% for TPA-based cell with an active area of 0.10 cm^2 was obtained from for efficiency certification (Fig. S19, ESI†). We calculated the integrated short-circuit current density (J_{sc}) for control and TPA-based PSCs for external quantum efficiency (EQE), the current of the target was a little higher than control (Fig. 5c). The target TPA-PSCs exhibit an open voltage (V_{oc}) of 1.203 V and fill factor (*FF*) of 84.35%, which is much higher than those of control (1.174 V and 79.43%) and Cz-based (1.185 V and 81.62%) devices (Fig. 5b and Table S4, ESI†). The enhanced cell performance of modified devices is attributed to the V_{oc} and *FF* originating from the efficient buried interface manipulation. Furthermore, we prepared the mini module to assess the positive function of TPA modifier (Fig. S20, ESI†). Photovoltaic results exhibit that a certified PCE of 22.83% is yielded for the TPA-based module with an aperture area of 11.44 cm^2, while the performance of active area with TPA is 23.83% (Fig. 5d, e and Fig. S21, ESI†), which is currently reported higher efficiency (Fig. 5f). Such a mini-module had a large FF of 82.02% as the certified highest FF for perovskite mini-modules (Table S5). Efficiency statistical analyses indicate that the modification of TPA has good repeatability (Table S6, ESI†). An efficiency of 21.91% was fabricated for large-area modules with an aperture area of 72.00 cm^2 (Fig. S22, S23 and Table S7, ESI†). Furthermore, the fabricated module with $Cs_{0.05}MA_{0.05}FA_{0.9}PbI_3$ perovskite system also achieved an efficiency of 23.37% (12.55 cm^2, Table S7, ESI†). Above results indicate that the introduced TPA lead to reduced interfacial charge recombination and lower PCE loss.

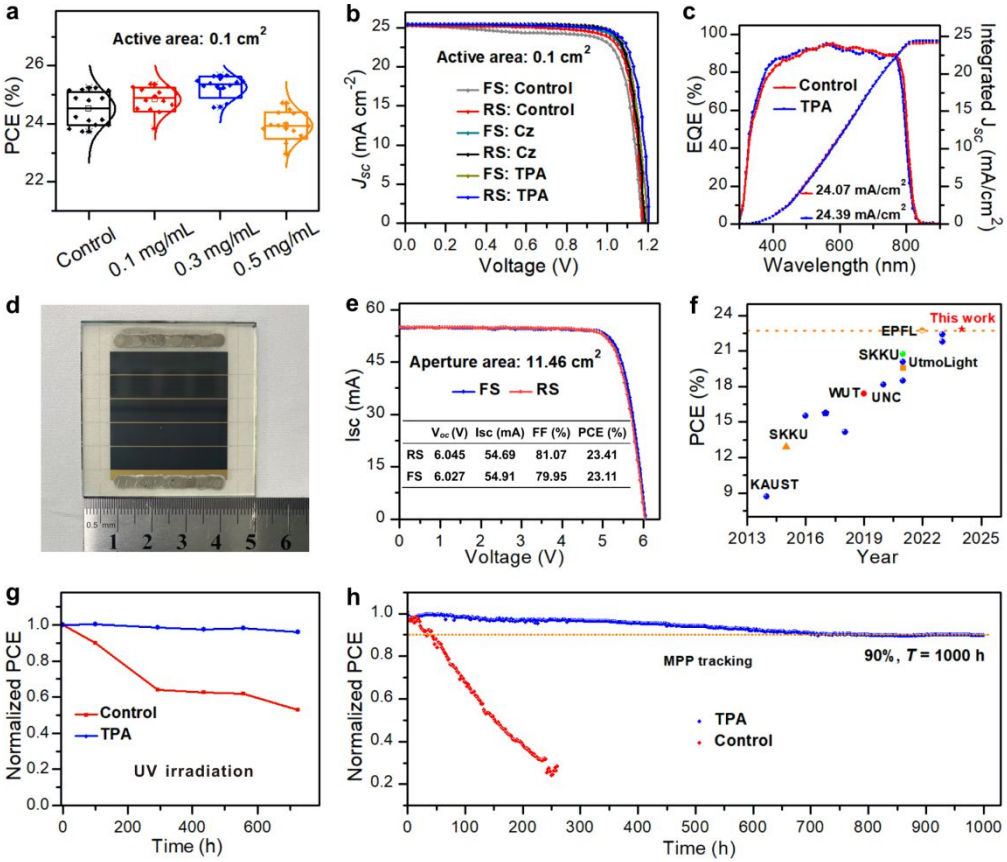

Fig. 5 (a) Efficiency statistics of cells treated with different concentration of TPA. (b) Best *J-V* data of champion devices for control and the devices with Cz and TPA. (c) EQE spectra of PSCs without and with TPA. (d) Photographs of 5 × 5 cm^2 mini module (e). I-V curves of TPA-based module and photovoltaic parameters. (f) Efficiency statistics chart for the module. (g). Long-term stability test of devices under UV light. (h). MPP tracking of devices under N_2 conditions with 25 °C.

We closely monitored the stability of the unencapsulated devices. Due to the poor moisture and thermal stability of devices with Spiro-OMeTAD as hole-transport material, we utilized an FTO/SnO_2/perovskite/phthalocyanine[58]/Au structure (Fig. S24, ESI†). Devices were firstly stored in a normal atmospheric environment with a relative humidity of 30% under UV light exposure (Fig. 5g). Reference device, after 700 hours of UV exposure, retained only 50% of the initial

This journal is © The Royal Society of Chemistry 20xx

Please do not adjust margins

efficiency. In contrast, TPA-treated device had a significant retention of 96% of the initial efficiency. The appearance images, XRD patterns, and SEM images for perovskite films before and after UV light irradiation (Fig. S25-27, ESI†) further reveal the improved UV stability of perovskite film based on TPA modification. This could be attributed to the TPA molecule compensating iodide vacancies and releases the interfacial lattice distortion at the buried interface, and effectively convert ultraviolet light into infrared light without damage to PSCs. This process further improves the light stability of PSCs. The long-term stability of both control and target devices operating at the maximum power point (MPP) was monitored for approximately 1000 hours under 1-sun illumination. As illustrated in Fig. 5h, the target device maintained approximately 90% of the initial efficiency, whereas the control sample had only around 20% of the initial efficiency. These findings indicate that it is important for enhancing the device stability by compensating the vacancies and releasing the interfacial lattice distortion at buried interface, particularly at simultaneous reduction of the UV corrosion effect.

Conclusions

Overall, we demonstrate that the introduction of cyano-based organic emitters can remarkably improve the efficiency and overall stability of the n-i-p structured PSCs. The cyano groups in emitters connect with the lead ion from perovskite to compensate the iodide vacancies and reinforce PbI_6 octahedral configuration at the buried interface. The champion device had a champion efficiency up to 25.67% for minimal small cells with the active area being 0.1 cm^2 and certified 22.8% for the mini module with an aperture area of 11.44 cm^2. Since the emitter molecule could effectively convert ultraviolet light into infrared light without damage to PSCs, the corresponding devices reveal the remarkably increased stability, especially for UV stability. Our work provides an in-depth understanding of buried interface manipulation and suggests a promising strategy for improving the performance and stability of PSCs.

Author Contributions

J. C. conceived the project; J. C. supervised and guided the project; Z.-Y. S. performed the fabrication, optimization and characterization of perovskite films and solar cells; G.-B. X. supervised all tests, data analysis, and summarized the findings; Z. S. assisted in conducting the in-situ GIWAXS experiments and performed data analysis; R. D. and X. M. carried out theoretical calculations; X. G and Y. W. participated in the discussion of the results. All authors participated experiment, discussed the results and contributed to the writing of the paper.

Conflicts of interest

There are no conflicts to declare.

Acknowledgements

This work was supported by the National Natural Science Foundation of China (22371096, 22075116 and 22221001), Fundamental Research Funds for the Central Universities of China (lzujbky-2021-ey10). Y.W. acknowledges funding support from the U.S. Department of Energy (Award No. DE-FG02-07ER46427). We also thank the beamlines BL14B1 and BL03HB at the Shanghai Synchrotron Radiation Facility for providing the beam time.

Notes and references

1. J. Park, J. Kim, H.-S. Yun, M. J. Paik, E. Noh, H. J. Mun, M. G. Kim, T. J. Shin and S. I. Seok, *Nature*, 2023, **616**, 724-730.
2. Z. Huang, Y. Bai, X. Huang, J. Li, Y. Wu, Y. Chen, K. Li, X. Niu, N. Li, G. Liu, Y. Zhang, H. Zai, Q. Chen, T. Lei, L. Wang and H. Zhou, *Nature*, 2023, **623**, 531-537.
3. Z. Liang, Y. Zhang, H. Xu, W. Chen, B. Liu, J. Zhang, H. Zhang, Z. Wang, D.-H. Kang, J. Zeng, X. Gao, Q. Wang, H. Hu, H. Zhou, X. Cai, X. Tian, P. Reiss, B. Xu, T. Kirchartz, Z. Xiao, S. Dai, N.-G. Park, J. Ye and X. Pan, *Nature*, 2023, **624**, 557-563.
4. Y. Zheng, Y. Li, R. Zhuang, X. Wu, C. Tian, A. Sun, C. Chen, Y. Guo, Y. Hua, K. Meng, K. Wu and C.-C. Chen, *Energy Environ. Sci.*, 2024, **17**, 1153-1162.
5. S. Yu, Z. Xiong, H. Zhou, Q. Zhang, Z. Wang, F. Ma, Z. Qu, Y. Zhao, X. Chu, X. Zhang and J. You, *Science*, 2023, **382**, 1399-1404.
6. S. Zhang, F. Ye, X. Wang, R. Chen, H. Zhang, L. Zhan, X. Jiang, Y. Li, X. Ji, S. Liu, M. Yu, F. Yu, Y. Zhang, R. Wu, Z. Liu, Z. Ning, D. Neher, L. Han, Y. Lin, H. Tian, W. Chen, M. Stolterfoht, L. Zhang, W.-H. Zhu and Y. Wu, *Science*, 2023, **380**, 404-409.
7. R. He, W. Wang, Z. Yi, F. Lang, C. Chen, J. Luo, J. Zhu, J. Thiesbrummel, S. Shah, K. Wei, Y. Luo, C. Wang, H. Lai, H. Huang, J. Zhou, B. Zou, X. Yin, S. Ren, X. Hao, L. Wu, J. Zhang, J. Zhang, M. Stolterfoht, F. Fu, W. Tang and D. Zhao, *Nature*, 2023, **618**, 80-86.
8. Best Research-Cell Efficiency Chart, https://www.nrel.gov/pv/cell-efficiency.html.
9. M. M. Lee, J. Teuscher, T. Miyasaka, T. N. Murakami and H. J. Snaith, *Science*, 2012, **338**, 643-647.
10. J. J. Yoo, G. Seo, M. R. Chua, T. G. Park, Y. Lu, F. Rotermund, Y.-K. Kim, C. S. Moon, N. J. Jeon, J.-P. Correa-Baena, V. Bulović, S. S. Shin, M. G. Bawendi and J. Seo, *Nature*, 2021, **590**, 587-593.
11. E. H. Anaraki, A. Kermanpur, L. Steier, K. Domanski, T. Matsui, W. Tress, M. Saliba, A. Abate, M. Grätzel, A. Hagfeldt and J.-P. Correa-Baena, *Energy Environ. Sci.*, 2016, **9**, 3128-3134.
12. Z. Ni, C. Bao, Y. Liu, Q. Jiang, W.-Q. Wu, S. Chen, X. Dai, B. Chen, B. Hartweg, Z. Yu, Z. Holman and J. Huang, *Science*, 2020, **367**, 1352-1358.
13. H. Min, D. Y. Lee, J. Kim, G. Kim, K. S. Lee, J. Kim, M. J. Paik, Y. K. Kim, K. S. Kim, M. G. Kim, T. J. Shin and S. Il Seok, *Nature*, 2021, **598**, 444-450.
14. S. Wu, J. Zhang, Z. Li, D. Liu, M. Qin, S. H. Cheung, X. Lu, D. Lei, S. K. So, Z. Zhu and A. K. Y. Jen, *Joule*, 2020, **4**, 1248-1262.

This journal is © The Royal Society of Chemistry 20xx

15. I. Levine, A. Al-Ashouri, A. Musiienko, H. Hempel, A. Magomedov, A. Drevilkauskaite, V. Getautis, D. Menzel, K. Hinrichs, T. Unold, S. Albrecht and T. Dittrich, *Joule*, 2021, **5**, 2915-2933.
16. Z. Qin, Y. Chen, X. Wang, N. Wei, X. Liu, H. Chen, Y. Miao and Y. Zhao, *Adv. Mater.*, 2022, **34**, 202203143.
17. Z. Xiong, X. Chen, B. Zhang, G. O. Odunmbaku, Z. Ou, B. Guo, K. Yang, Z. Kan, S. Lu, S. Chen, N. A. N. Ouedraogo, Y. Cho, C. Yang, J. Chen and K. Sun, *Adv. Mater.*, 2022, **34**, 202106118.
18. Y. Dong, W. Shen, W. Dong, C. Bai, J. Zhao, Y. Zhou, F. Huang, Y. B. Cheng and J. Zhong, *Adv. Energy Mater.*, 2022, **12**, 202200417.
19. T. Liu, X. Zhao, X. Zhong, Q. C. Burlingame, A. Kahn and Y.-L. Loo, *ACS Energy Lett.*, 2022, **7**, 3531-3538.
20. C. Chen, H. Li, J. Jin, X. Chen, Y. Cheng, Y. Zheng, D. Liu, L. Xu, H. Song and Q. Dai, *Adv. Energy Mater.*, 2017, **7**, 201700758.
21. W. Li, W. Zhang, S. Van Reenen, R. J. Sutton, J. Fan, A. A. Haghighirad, M. B. Johnston, L. Wang and H. J. Snaith, *Energy Environ. Sci.*, 2016, **9**, 490-498.
22. C. Fu, Z. Gu, Y. Tang, Q. Xiao, S. Zhang, Y. Zhang and Y. Song, *Angew. Chem. Int. Ed.*, 2022, **61**, e202117067.
23. X. Zhu, C. F. J. Lau, K. Mo, S. Cheng, Y. Xu, R. Li, C. Wang, Q. Zheng, Y. Liu, T. Wang, Q. Lin and Z. Wang, *Nano Energy*, 2022, **103**, 107849.
24. X. Zhuang, D. Zhou, S. Liu, R. Sun, Z. Shi, L. Liu, T. Wang, B. Liu, D. Liu and H. Song, *Adv. Energy Mater.*, 2022, **12**, 202200614.
25. J. Wei, Q. Wang, J. Huo, F. Gao, Z. Gan, Q. Zhao and H. Li, *Adv. Energy Mater.*, 2020, **11**, 202002326.
26. J. Cao, X. Lv, P. Zhang, T. T. Chuong, B. Wu, X. Feng, C. Shan, J. Liu and Y. Tang, *Adv. Mater.*, 2018, **30**, 201800568.
27. S. S. Shin, E. J. Yeom, W. S. Yang, S. Hur, M. G. Kim, J. Im, J. Seo, J. H. Noh and S. I. Seok, *Science*, 2017, **356**, 167-171.
28. L. Deng, H. Wang, S. Rafique, Y. Wang, T. Hu, K. Liu, Y. Wang, X. Li, Z. Xie, J. Tang, Z. Liu, J. Li, W. Yuan, J. Wang, A. Yu and Y. Zhan, *Adv. Funct. Mater.*, 2023, **33**, 202303742.
29. Y. Wang, Z. Zhang, Y. Lan, Q. Song, M. Li and Y. Song, *Angew. Chem. Int. Ed.*, 2021, **60**, 8673-8677.
30. H. Guo, W. Xiang, Y. Fang, J. Li and Y. Lin, *Angew. Chem. Int. Ed.*, 2023, **62**, e202304568.
31. H. Cui, L. Huang, S. Zhou, C. Wang, X. Hu, H. Guan, S. Wang, W. Shao, D. Pu, K. Dong, J. Zhou, P. Jia, W. Wang, C. Tao, W. Ke and G. Fang, *Energy Environ. Sci.*, 2023, **16**, 5992-6002.
32. R. Xu, F. Pan, J. Chen, J. Li, Y. Yang, Y. Sun, X. Zhu, P. Li, X. Cao, J. Xi, J. Xu, F. Yuan, J. Dai, C. Zuo, L. Ding, H. Dong, A. K. Y. Jen and Z. Wu, *Adv. Mater.*, 2023, **36**, 202308039.
33. J. Dou, C. Zhu, H. Wang, Y. Han, S. Ma, X. Niu, N. Li, C. Shi, Z. Qiu, H. Zhou, Y. Bai and Q. Chen, *Adv. Mater.*, 2021, **33**, 202102947.
34. J. H. Lee, S. Lee, T. Kim, H. Ahn, G. Y. Jang, K. H. Kim, Y. J. Cho, K. Zhang, J.-S. Park and J. H. Park, *Joule*, 2023, **7**, 380-397.
35. X. Wang, H. Huang, M. Wang, Z. Lan, P. Cui, S. Du, Y. Yang, L. Yan, Q. Zhang, S. Qu and M. Li, *Adv. Mater.*, 2024, **36**, 202310710.
36. S. Chen, X. Dai, S. Xu, H. Jiao, L. Zhao and J. Huang, *Science*, 2021, **373**, 902-907.
37. H. Su, Z. Xu, X. He, Y. Yao, X. Zheng, Y. She, Y. Zhu, J. Zhang and S. Liu, *Adv. Mater.*, 2023, **36**, 202306724.
38. H. Hu, D. B. Ritzer, A. Diercks, Y. Li, R. Singh, P. Fassl, Q. Jin, F. Schackmar, U. W. Paetzold and B. A. Nejand, *Joule*, 2023, **7**, 1574-1592.
39. W. Meng, K. Zhang, A. Osvet, J. Zhang, W. Gruber, K. Forberich, B. Meyer, W. Heiss, T. Unruh, N. Li and C. J. Brabec, *Joule*, 2022, **6**, 458-475.
40. C. Luo, G. Zheng, F. Gao, X. Wang, C. Zhan, X. Gao and Q. Zhao, *Nat. Photon.*, 2023, **17**, 856-864.
41. H. Li, C. Zhang, C. Gong, D. Zhang, H. Zhang, Q. Zhuang, X. Yu, S. Gong, X. Chen, J. Yang, X. Li, R. Li, J. Li, J. Zhou, H. Yang, Q. Lin, J. Chu, M. Grätzel, J. Chen and Z. Zang, *Nat. Energy*, 2023, **8**, 946-955.
42. Y. Zhang, Q. Song, G. Liu, Y. Chen, Z. Guo, N. Li, X. Niu, Z. Qiu, W. Zhou, Z. Huang, C. Zhu, H. Zai, S. Ma, Y. Bai, Q. Chen, W. Huang, Q. Zhao and H. Zhou, *Nat. Photon.*, 2023, **17**, 1066-1073.
43. N. Li, S. Tao, Y. Chen, X. Niu, C. K. Onwudinanti, C. Hu, Z. Qiu, Z. Xu, G. Zheng, L. Wang, Y. Zhang, L. Li, H. Liu, Y. Lun, J. Hong, X. Wang, Y. Liu, H. Xie, Y. Gao, Y. Bai, S. Yang, G. Brocks, Q. Chen and H. Zhou, *Nat. Energy*, 2019, **4**, 408-415.
44. M. A. Uddin, P. J. S. Rana, Z. Ni, G. Yang, M. Li, M. Wang, H. Gu, H. Zhang, B. D. Dou and J. Huang, *Nat. Commun.*, 2024, **15**.
45. X. Ji, L. Bi, Q. Fu, B. Li, J. Wang, S. Y. Jeong, K. Feng, S. Ma, Q. Liao, F. R. Lin, H. Y. Woo, L. Lu, A. K. Y. Jen and X. Guo, *Adv. Mater.*, 2023, **35**, 202303665.
46. F. Zhang, B. Tu, S. Yang, K. Fan, Z. Liu, Z. Xiong, J. Zhang, W. Li, H. Huang, C. Yu, A. K. ‐ Y. Jen and K. Yao, *Adv. Mater.*, 2023, **35**, 202303139.
47. R. Azmi, D. S. Utomo, B. Vishal, S. Zhumagali, P. Dally, A. M. Risqi, A. Prasetio, E. Ugur, F. Cao, I. F. Imran, A. A. Said, A. R. Pininti, A. S. Subbiah, E. Aydin, C. Xiao, S. I. Seok and S. De Wolf, *Nature*, 2024, **628**, 93-98.
48. Y. Li, P. Han, X. Zhang, J. Zhou, X. Qiao, D. Yang, A. Qin, B. Z. Tang, J. Peng and D. Ma, *J. Mater. Chem. C*, 2023, **11**, 3284-3291.
49. X. Guo, P. Yuan, J. Fan, X. Qiao, D. Yang, Y. Dai, Q. Sun, A. Qin, B. Z. Tang and D. Ma, *Adv. Mater.*, 2021, **33**, 202006953.
50. C. Zhang, Y. Son, H. Kim, S.-H. Lee, X. Liang, G. Fu, S.-U. Lee, D.-A. Park, Q. Jiang, K. Zhu and N.-G. Park, *Joule*, 2024, **8**, 10.1016/j.joule.2024.1002.1015.
51. C. Chen, X. Wang, Z. Li, X. Du, Z. Shao, X. Sun, D. Liu, C. Gao, L. Hao, Q. Zhao, B. Zhang, G. Cui and S. Pang, *Angew. Chem. Int. Ed.*, 2021, **61**, e202113932.
52. Y. Wang, Y. Yang, N. Li, M. Hu, S. R. Raga, Y. Jiang, C. Wang, X. L. Zhang, M. Lira ‐ Cantu, F. Huang, Y. B. Cheng and J. Lu, *Adv. Funct. Mater.*, 2022, **32**, 202204396.
53. Y. Yang, C. Liu, Y. Ding, B. Ding, J. Xu, A. Liu, J. Yu, L. Grater, H. Zhu, S. S. Hadke, V. K. Sangwan, A. S. R. Bati, X. Hu, J. Li, S. M. Park, M. C. Hersam, B. Chen, M. K. Nazeeruddin, M. G. Kanatzidis and E. H. Sargent, *Nat. Energy*, 2024, **9**, 316-323.
54. H. Meng, S. Yuan, Z. Zhu, W. Chen, J. Xu, K. Mao, T. Li, X. Feng, C. Xiao, F. Cai, F. Cao, W. Peng, J. Xu, X. Wu, Z. Su, K. Zhang, Y. Gao, M. D. McGehee and J. Xu, *Nat. Energy*, 2024, DOI: 10.1038/s41560-024-01471-4.
55. T. Bu, J. Li, H. Li, C. Tian, J. Su, G. Tong, L. K. Ono, C. Wang, Z. Lin, N. Chai, X.-L. Zhang, J. Chang, J. Lu, J. Zhong, W.

This journal is © The Royal Society of Chemistry 20xx

Please do not adjust margins

Huang, Y. Qi, Y.-B. Cheng and F. Huang, *Science*, 2021, **372**, 1327-1332.

56. H. Min, S.-G. Ji and S. I. Seok, *Joule*, 2022, **6**, 2175-2185.

57. Z. Fang, L. Wang, X. Mu, B. Chen, Q. Xiong, W. D. Wang, J. Ding, P. Gao, Y. Wu and J. Cao, *J. Am. Chem. Soc.*, 2021, **143**, 18989-18996.

58. Z. Yu, L. Wang, X. Mu, C. C. Chen, Y. Wu, J. Cao and Y. Tang, *Angew. Chem. Int. Ed.*, 2021, **60**, 6294-6299.